Cooperative catalytic performance of bimetallic Ni-Au nanocatalyst for highly efficient hydrogenation of nitroaromatics and corresponding mechanism insight

Lei Qin [a,1], Zhuotong Zeng [b,1], Guangming Zeng [a,1,∗], Cui Lai [a,∗], Abing Duan [a,∗], Rong Xiao [b,∗], Danlian Huang [a], Yukui Fu [a], Huan Yi [a], Bisheng Li [a], Xigui Liu [a], Shiyu Liu [a], Mingming Zhang [a], Danni Jiang [a]

[a] *College of Environmental Science and Engineering, Hunan University and Key Laboratory of Environmental Biology and Pollution Control(Hunan University), Ministry of Education, Changsha 410082, PR China*

[b] *Department of Dermatology, Second Xiangya Hospital, Central South University, Changsha 410011, PR China*

∗ Corresponding author at: College of Environmental Science and Engineering, Hunan University, Changsha, Hunan 410082, China. E-mail address: zgming@hnu.edu.cn (G.M. Zeng) ,laicui@hnu.edu.cn (C.Lai) , duanabing@hnu.edu.cn (A. Duan) and xiaorong65@csu.edu.cn (R. Xiao).

[1] These authors contribute equally to this article.

Abstract

HNO_3-modified carbon black supported Ni-Au bimetallic nanocatalysts (HCB-Ni-Au) with different Ni/Au molar ratio were synthesized for hydrogenation of nitroaromatics. The synergistic effect between bimetallic nanoparticles and HCB, Ni and Au nanoparticles improved the catalytic efficiency. The reaction mechanism and pathway investigation exhibited that nitroaromatics were reduced by cleavage of –N=O bond and azo linkage (–N=N–) and uptake of H from Ni-H and Au-H bonds. Density functional theory theoretical calculation showed 4-nitrophenol (4-NP) with higher free energy was easier to be catalyzed. The activation of enthalpy for MO was 65.7 kcal $\cdot$mol^{-1}, which displayed the highest catalytic rate of 2.1055 min^{-1}. Meanwhile, the reaction rate of 4-NP hydrogenation catalyzed by HCB-Ni_6-Au_1 reached 1.9617 min^{-1}, which was 15 and 38 times higher than that of Ni and Au monometallic nanocatalyst, respectively. HCB-Ni_6-Au_1 with good structural stability could be well reused and applied in tap, distilled, river, and lake water samples.

Keywords: Bimetallic nanocatalysts; Carbon black; Density functional theory; Nitroaromatics; Hydrogenation.

1. Introduction

Nowadays, industrialization has created unprecedented material wealth for us but brought serious trauma for ecological environment [1-5]. Water pollution is one of the most important environmental threats because of its universality and high risk [6-13]. Nitroaromatics, including nitrophenols and some of azo-dyes, are dangerous organic pollutants from industry and agriculture [14-16]. They are widely used in leather, plastic, pharmaceuticals, pesticides and paper industries and have been considered to result in significant damage to water environment [17, 18]. Nitroaromatics are difficult to completely remove owing to the strong photo- and thermal stability and the resistance to biodegradation [19]. If accumulated over a long period of time, the human body can be damaged [20]. Therefore, efficient methods are necessary to degrade or decolourize these compounds. In this case, the catalytic hydrogenation is considered as the most effective one because of the strong operability and high efficiency. In addition, the products of hydrogenation, taking aminophenols as examples, are useful precursors for the synthesis of drugs, drying agent and corrosion inhibitor, which can bring economic benefits.

Notably, noble metal nanoparticles like platinum, gold, and silver nanoparticles (Pt, Au, and Ag NPs) based homogeneous and heterogeneous catalysts are well-reported as highly efficient catalysts for the hydrogenation of nitroaromatics [21-25]. However, the high price of them inevitably restrict the industrial production and wide application [26-29]. In this case, the bimetallic combination with transition metal is a good choice to solve this problem, and the catalytic efficiency can be enhanced because of the synergistic effect between different metals [30, 31]. On the other hand, some supports like carbon materials and metallic oxides are gained much attention because they can form hybrid nanostructures with metal NPs, thus controlling the size of metal particles and enhancing the stability and catalytic activity because of synergistic effects [32-37]. For example, Das et al. [38] synthesized a Ag NPs decorated magnetic polypyrrole nanocomposite without the addition of reductive agent or stabilizer for highly efficient reduction of 4-nitrophenol (4-NP) and organic dyes. Recently, Fu et al. [39] and Nguyen et al. [40] both used graphitic carbon nitride as support to deposit Au NPs for the catalytic reduction of nitrophenols and obtained excellent catalytic activity and stability. In this case, carbon black (CB), as one kind of carbon material, is good candidate for the support of metal NPs due to its turbostratic structures with high conductivity and surface area, excellent chemical and mechanical stability, as well as its low cost and easy availability.

According to our previous report, CB has plenty of pore structures and is easy to aggregate, which provide hierarchical porous structure [41]. This is beneficial for the adsorption of nitrophenols and dyes, which contributes to the catalytic reaction. As for the CB supported Au catalyst, the fast electron transfer from CB to Au NPs also improves the catalytic efficiency. However, the low content of oxygen-containing groups on the surface of CB indeed decreases the amount of anchored Au NPs. Besides, the weak hydrophilcity also limits the application of Au/CB catalyst in water environment. In this case, some researchers enhanced the surface properties of CB by modifying or doping [42, 43]. Although there are many reports studied the modified carbon materials supported noble metal catalysts for the hydrogenation of nitroaromatics, they just simply reported the catalytic efficiency of these catalysts. The reaction mechanism and pathway are lack of investigation. Meanwhile, considering the catalysts exhibited different catalytic hydrogenation efficiency towards different nitroaromatics, most of reports explained it intangibly or theoretically. As one kind of new technique, the density functional theory (DFT) theoretical calculation has been widely used to explain experimental phenomenon and guide the design of experiment in recent years, while it was rarely used for the study of nitroaromatics hydrogenation. Thus, further investigation on the hydrogenation of nitroaromatics with the assistant of both experimental operation and theoretical calculation is necessary.

Hence, we successfully prepared HNO_3-modified CB supported bimetallic Ni-Au nanocatalysts (HCB-Ni-Au) for highly catalytic hydrogenation of nitroaromatics and creatively combined experimental results and DFT theoretical calculation to investigate the reason for different catalytic efficiency of different nitroaromatics. The mechanism, possible pathway, and catalytic efficiency were studied. In addition, the comparison of HCB supported monometallic Au and Ni nanocatalysts was proposed. The comparison on the characteristics of CB and study for the effects on catalytic activity by modification or doping was also conducted. The physicochemical properties of prepared catalysts were detected by transmission electron microscopy (TEM), X-ray diffraction (XRD), specific surface area and porosity (BET), X-ray photoelectron spectroscopy (XPS), H_2-temperature programmed reduction (H_2-TPR), inductively coupled plasma optical emission spectrometer (ICP-OES), and Electron paramagnetic resonance (EPR). The crystalline structure of HCB-Ni-Au nanocatalyst before and after reaction was studied either. The universality and practical application of as-prepared HCB-Ni-Au as well as the ions and pH effects were further conducted. The combination of experiment and theoretical calculation can better consider the intrinsic properties of pollutants and provide guidance for highly efficient removal of them in water environment.

2. Experimental

2.1. Preparation of HCB-Ni, HCB-Ni-Au, and HCB-Au nanocatalysts

The synthetic process of HCB-Ni-Au nanocatalysts is shown in **Scheme 1**. Typically, pristine CB was firstly washed with water and ethanol for several times and dried in oven for 12 h before use. To improve the hydrophility and adsorptivity of metal NPs, 2.0 g of CB and 200 mL concentrated HNO_3 were mixed in a 250 mL conical flask. The mixture was heated at 85 ℃ with continuously stirring for 12 h. The resulting HCB was diluted and washed with ultrapure water until neutral, and finally dried for further use.

The synthesis of HCB-Ni catalyst is as follows: 200 mg of HCB was mixed with 75 mL of EG and sonicated for 30 min for further dispersion. Subsequently, a certain amount of $NiCl_2$-EG solution (1-5 mL, 24.26 mM) was added drop by drop and vigorously stirred for 15 min. Then, 25 mL of NaOH (1 M) was added, followed by the gradual addition of 5 mL of $N_2H_4 \cdot H_2O$. The mixture was transferred to the water bath and heated to 80 ℃ with stirring. After reaction at 80 ℃ for 2 h, the resulting HCB-Ni nanocatalyst was separated by filtration, washed with ethanol and water for several times and finally dried in an oven at 60 ℃ for further use.

The preparation of different proportions of HCB-Ni-Au bimetallic nanocatalyst was proposed on the basis of HCB-Ni synthesis. Typically, 200 mg of as-prepared HCB-Ni was added into 100 mL of EG and adequately dispersed by ultrasonic treatment for 30 min. Then, the suspension was heated at 90 ℃ with thorough stirring and 0.5 mL of $HAuCl_4$ solution was added into the suspension, followed by quick addition of 200 μL of $N_2H_4 \cdot H_2O$. After the reaction of 3 h, the resulting HCB-Ni-Au bimetallic nanocatalyst was filtered, washed with ethanol and water for several times and finally dried in an oven at 60 ℃. The molar ratio of Ni and Au is from 2:1 to 10:1, in which the catalysts were denoted as HCB-Ni_2-Au_1 to HCB-Ni_{10}-Au_1 respectively. The preparation of HCB-Au was as the same with the procedure of Au reduction in HCB-Ni-Au preparation (HCB was used to replace HCB-Ni).

2.2. Catalytic test

To study the catalytic activity of prepared HCB-Ni-Au nanocatalysts, reduction of phenols and azo dyes with NaBH$_4$ was proposed at ambient temperature. 4-NP served as the model target. The catalytic activity of HCB supported monometallic Au, Ni and HCB supported bimetallic Ni-Au nanocatalysts (HCB-Ni-Au) was performed as the procedure of 4-NP hydrogenation by HCB-Ni-Au. Typically, 4-NP (50 mL, 0.2 mM) was freshly prepared and HCB-Ni-Au catalyst (5 mg) was added under continuous stirring for 30 min to reach the adsorption-desorption equilibrium. A certain amount of NaBH$_4$ (50 times over 4-NP) was added with stirring. 3 mL of solution was taken at specified time intervals and filtered through a 0.22 μm filter membrane. The catalytic performance was evaluated by measuring the solution on UV-Vis spectrometry. After reaction, the catalyst was removed by filtration and washed with ultrapure water and ethanol for several times, then reused for 8 times. In addition, the catalytic activity of HCB-Ni-Au nanocatalyst on other phenols and azo dyes like 2-nitrophenol (2-NP), 3-nitrophenol (3-NP), methyl orange (MO), eriochrome black T (EBT) and Congo red (CR) was explored as the same procedure of 4-NP reduction in ultrapure water by HCB-Ni$_6$-Au$_1$ (5 mg) and NaBH$_4$ (50 times over 4-NP). Finally, the catalytic activity of HCB-Ni-Au nanocatalyst on different water sources including tap water, distilled water, river water, and lake water (collected from convenience store, our laboratory, Hsiang River (Changsha, China), and Lake of Peach, respectively) was investigated. These samples were firstly filtered through a 0.22 μm syringe filter to remove impurities. Secondly, the UV-Vis spectra were proposed to determine the background concentration of 4-NP. Finally, these samples were spiked with standard solution of 4-NP (0.2 mM). The catalytic activity was performed as the reduction of 4-NP in ultrapure water by HCB-Ni$_6$-Au$_1$ (5 mg) and NaBH$_4$ (50 times over 4-NP). Three parallel experiments were carried out for all procedure.

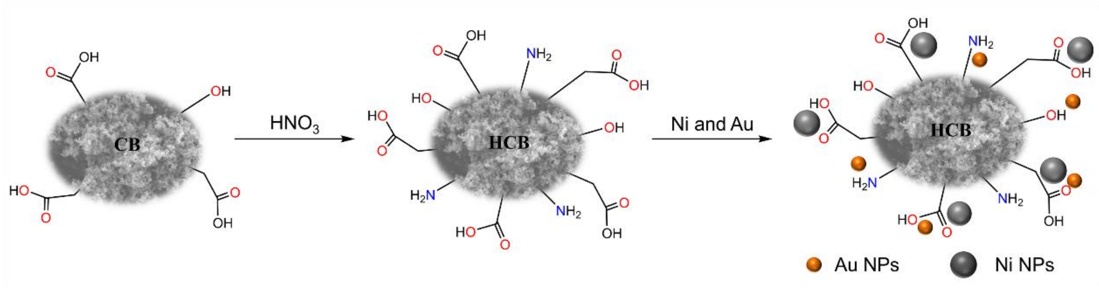

Scheme 1. The synthetic process of HNO_3 modified CB supported Ni-Au bimetallic nanocatalysts.

3. Results and discussion

3.1. Characterization of catalysts

In order to explore the crystal structures and chemical compositions, XRD studies of prepared nanocatalysts were carried out. As shown in **Fig.1a**, the diffraction pattern of HCB shows two characteristic peaks at 24.5 ° and 43.6 °, which are attributed to the (002) and (101) plane reflection of carbon materials [31]. Other well-defined diffraction peaks of HCB-Au located at 38.0 °, 44.0 °, 64.6 ° and 77.7 ° and HCB-Ni located at 44.4 °, 51.7 ° and 76.3 ° are due to the (111), (200), (220) and (311) crystal plane reflections of Au (JCPDS 04-0784) and the (111), (200) and (220) crystal plane reflections of Ni (JCPDS 04-0850) respectively. With the deposition of both Au NPs and Ni NPs, the characteristic peak of (002) reflection for HCB is broad and weak and that of (101) plane is not displayed. This may be because the deposition of Au NPs and Ni NPs weakens the internal structure order of HCB and the peak of Au in (200) covers the (101) plane of HCB. Interestingly, the peak of Au (111) becomes narrow and the intensity of that increases. This is possibly because the size of Au NPs decreases and more Au NPs are deposited due to the presence of Ni NPs. Meanwhile, the peak intensity of Ni (111) increases because of the peak overlap with Au (200). In addition, with the increasing molar ratio of Ni and Au, the characteristic peaks of HCB (002) reflection is broad and weak, the peaks of Au (111) are decreased and that of Ni NPs are increased accordingly (**Fig.1**b). These results prove the successful deposition of both Ni NPs and Au NPs on HCB and the increasing content of Ni.

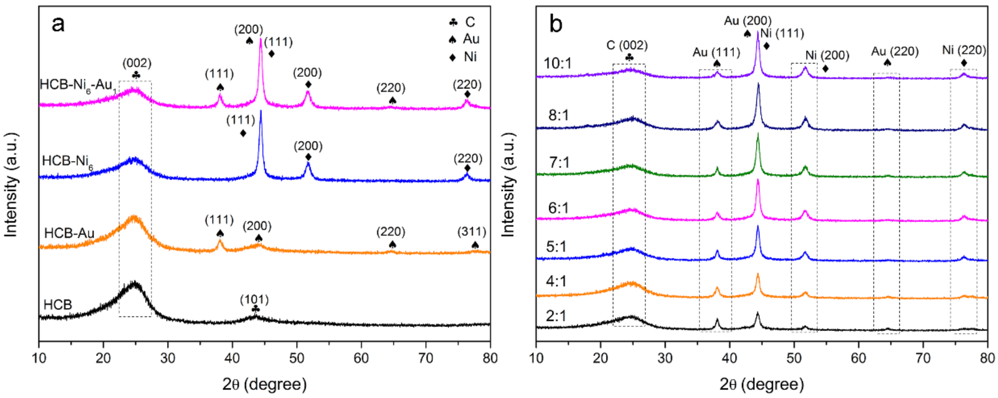

Fig. 1. XRD patterns of (a) HCB, HCB-Au, HCB-Ni$_6$ and HCB-Ni$_6$-Au$_1$ nanocatalysts; (b) HCB-Ni-Au bimetallic nanocatalysts with different molar ratio of Ni and Au (2:1-10:1).

The morphology and microstructure of HCB, HCB-Au, HCB-Ni, and HCB-Ni$_6$-Au$_1$ bimetallic nanocatalyst were investigated by TEM characterization. As exhibited in **Fig. 2**a, HCB has an approximately spherical structure with the size of 30 nm. The crystal plane (002) with the lattice space of 0.34 nm is due to the plane between two single graphene layers in HCB (**Fig. 2**f). The analysis of HCB-Au and HCB-Ni$_6$ nanocatalyst indicates that Au NPs and Ni NPs are successfully deposited on HCB (**Fig. 2**b-c) respectively. The high resolution TEM (HR-TEM) images showed in **Fig. 2**g-h clearly suggests the lattices of Au NPs and Ni NPs with spaces of 0.236 nm and 0.208 nm, 0.248 nm and 0.178 nm, which are attributed to the (111) plane of Au NPs and (111), (110) and (200) planes of Ni NPs. After the deposition of both Au NPs and Ni NPs, the TEM and HR-TEM images show that spherical Au NPs and irregular Ni NPs are well anchored on the surface of HCB (**Fig. 2**d-e). The mapping images and Energy Dispersive X-ray spectroscopy (EDX) of HCB-Ni$_6$-Au$_1$ suggest C, N, O, Ni and Au elements in here (**Fig. 2**i-j and **Fig. S1**). Interestingly, it is found that more Au NPs are formed in HCB-Ni_6-Au_1 and the size of that is much smaller than Au NPs formed in HCB-Au (**Fig. S2**). As shown in **Fig. S2**b and d, the mean size of Au NPs in HCB-Ni_6-Au_1 is below 12 nm, while it in HCB-Au is about 28.16 and 31.10 nm. We speculate that the presence of Ni NPs may be conducive to the formation of Au NPs crystals and lead to smaller size of Au NPs. This may be attributed to the hydrogen spillover phenomenon between Au and NiO [44, 45]. In addition, Au NPs in HCB-Ni_6-Au_1 seem to prefer growing near the Ni NPs, and some of them even deposit on the edge of Ni NPs. This is possibly because metal Au tends to contact with Ni to form Ni-Au nanocomposites in the presence of Ni NPs [46]. It is well known that Au NPs are easier to form with oxygen-containing materials and can firmly attach on the surface of them because of the Au-O bond [47-49]. In this paper, there are also NiO and $Ni(OH)_2$ present because the surface atoms on Ni NPs can be easily oxidized in air with the existence of water (XPS data). Thus Au NPs may be grown near the Ni NPs. Another interesting thing is that the formation process of Au NPs can promote the reduction of residuary Ni^{2+} to Ni^0 because the redox pair potential of Au^{3+}/Au (1.8 V) is higher than that of Ni^{2+}/Ni (−0.246 V) [50, 51]. The formed Au nuclei can further induce the reduction of Ni^{2+}/Ni by the electron transfer process (equation 1-2).

$$2Au^0 + 3Ni^{2+} \rightarrow 2Au^{3+} + 3Ni^0 \quad (1)$$

$$Au^{3+} + e^- \rightarrow Au^0 \quad (2)$$

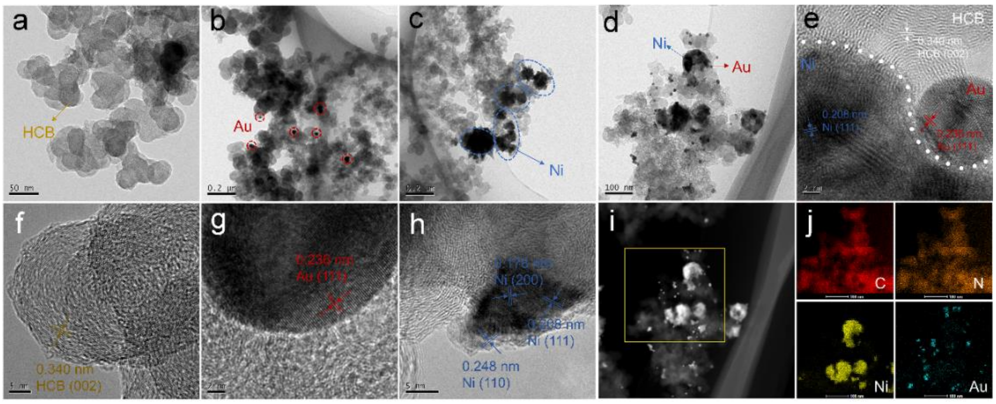

Fig. 2. TEM and HRTEM images of HCB (a and f), HCB-Au (b and g), HCB-Ni_6 (c and h) and HCB-Ni_6-Au_1 (d and e); STEM and mapping of HCB-Ni_6-Au_1 nanocatalyst (i and j).

The XPS spectra of CB, HCB, and HCB-Ni_6-Au_1 presented in **Fig. 3**a illustrate that C and O are the primary elements in here. The fitted C 1s spectra are shown in **Fig. 3**b. There are four peaks located at 284.73, 285.38, 287.7, and 290.00 eV in CB, which are assigned to the sp^2, sp^3 carbon, C=O bond and π-π^* transition loss, respectively [42]. However, two peaks contributing to C-N and C(=O)O bonds (around 286.8 and 289.2 eV) show up in HCB and HCB-Ni_6-Au_1 [52, 53]. The content of O is very low in CB and is much higher in HCB (**Fig. 3**c). Simultaneously, a certain of N also exists in HCB (**Fig. 3**d). This benefits from the modification of HNO_3, which brings plenty of O and introduces the doping of N. This is conducive to the deposition of Au and Ni NPs. The global XPS spectrum also shows the elements of Ni and Au in HCB-Ni_6-Au_1 (**Fig. 3**e). The high-resolution spectra of Au 4f illustrate two main peaks at 84.54 and 88.19 eV, which are typical values of Au in zero oxidation state (**Fig. 3**f). Besides, a peak at 90.45 eV assigned to the Au(III) oxidation state is observed, which means the Au(III) has not been reduced completely. The Ni spectral feature in HCB-Ni_6-Au_1 contains metallic Ni, Ni oxide and Ni hydroxide (**Fig. 3**g). Generally, a complex structure with intense satellite signals adjacent to the main peak is observed in the Ni 2p spectrum. The peaks located at 852.77 eV is attributed to metallic Ni, the intense doublet located at 856.20 and 861.76 eV is ascribed to Ni^{2+} in NiO [54]. The second doublet located at 873.70 and 880.00 eV is because of the Ni^{2+} in $Ni(OH)_2$. It is noteworthy that the peaks of NiO and $Ni(OH)_2$ are not shown in XRD patterns and this is possibly because the resulting NiO and $Ni(OH)_2$ are amorphous.

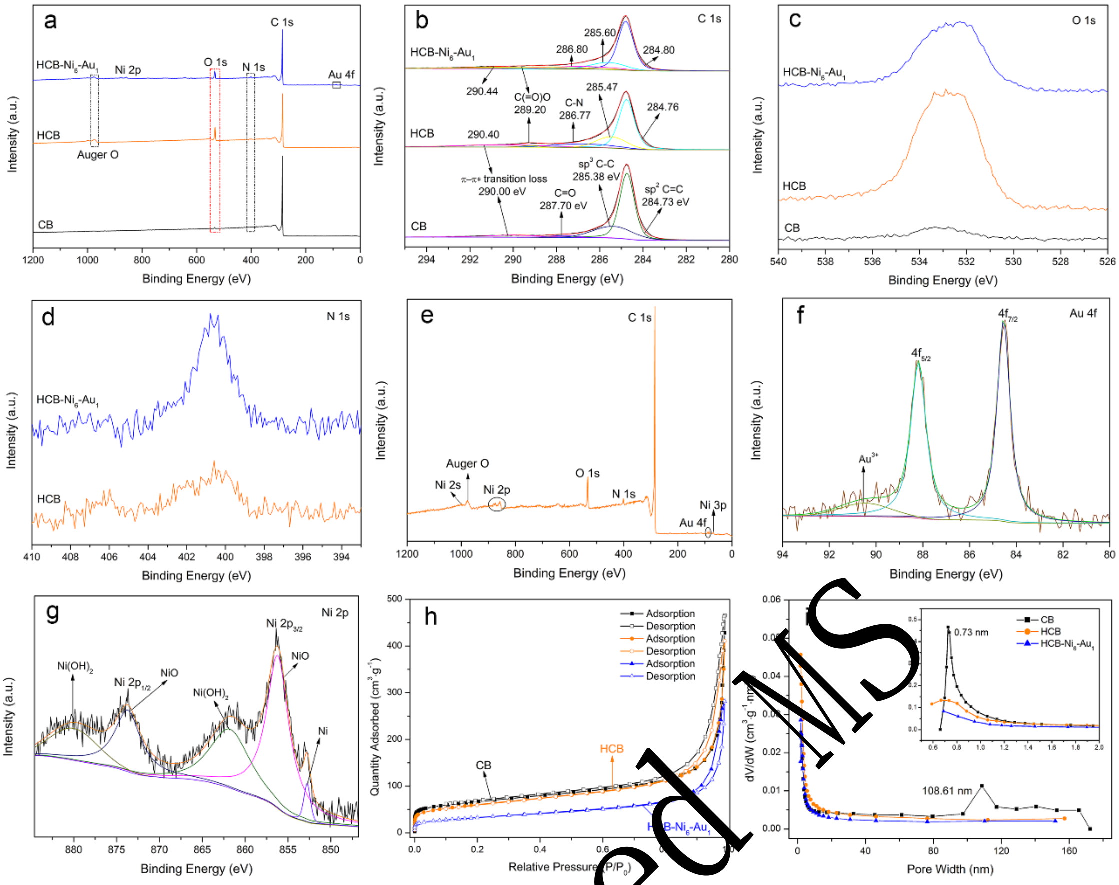

Fig. 3. XPS survey spectra (a) and high-resolution spectra for C 1s (b) and O 1s (c) of CB, HCB, and HCB-Ni$_6$-Au$_1$; XPS high-resolution spectra for N 1s (d) of HCB and HCB-Ni$_6$-Au$_1$; XPS survey spectrum (e) and high-resolution spectra for Au 4f (f) and Ni 2p (g) of HCB-Ni$_6$-Au$_1$. Nitrogen adsorption-desorption isotherms (h), BJH pore size distribution (i), and micropore pore size distribution (inset of i) of CB, HCB, and HCB-Ni$_6$-Au$_1$.

The surface area and pore size distribution of CB, HCB, and HCB-Ni$_6$-Au$_1$ were measured by BET. The nitrogen adsorption-desorption isotherms of them follow the typical IUPAC type IV pattern with a H_3 hysteresis, suggesting the existence of mesopores in them (**Fig. 3**h). In the meantime, plenty of micropores exist in CB and it decreases slightly after the modification of HNO_3, while decreases apparently after the deposition of Ni and Au NPs. BJH pore size distribution and micropore pore size distributions of CB, HCB, and HCB-Ni$_6$-Au$_1$ were further measured. The results demonstrate that the main pore size contributions of CB are macropore of 108.61 nm and micropore of 0.73 nm (**Fig. 3**i). This suggests there is also macropore structure in CB. However, the modification process by HNO_3 changes the pore size contribution, which reduces the contribution of macropore and micropore and enhances the contribution of mesopore (**Table S1**). It can also be demonstrated by the results of the specific surface area analysis in which the external surface area of CB increases from 155.94 to 179.01 m^2 g^{-1}, the microporous area decreases from 75.17 to 34.09 m^2 g^{-1}, and the total pore volume and average pore size decrease from 0.82 to 0.64 cm^3 g^{-1} and 26.85 to 13.19 nm respectively. After the deposition of monometallic Ni, Au NPs or even bimetallic Ni and Au NPs on HCB, the BET surface area (S_{BET}), external surface area, microporous area, and total pore volume are almost all decreased. However, the average pore size of them are increased, which may be because the deposition of metallic NPs brings some new pores in metallic NPs or between the metallic NPs and HCB. Interestingly, the deposition of Au NPs alone increases the microporous area. One of the possible reason is that part of small size of Au NPs entered the macropore or mesopore of HCB during deposition, which reduced the size of macropore or mesopore. Another possible reason is the small size of Au NPs also brings some micropores.

The H_2-TPR of prepared nanocatalysts was used to determine the interaction between active component and the effect of the activation process on the reaction of hydrogenation. The H_2-TPR measurements carried out for CB, HCB, HCB-Au, HCB-Ni_6 and HCB-Ni_6-Au_1 are shown in **Fig. S3** and the H_2 consumption values of different peaks for them are exhibited in **Table S2**. There are two reduction peaks ranging from 400 to 500°C and 600 to 700°C for the H_2-TPR test of CB and HCB, which are caused by the reduction of surface oxygen and methanation process of carbon [44]. After the modification of CB by HNO_3, the intensity of reduction peaks increase with an increasing H_2 consumption and the peak around 600 to 700°C shifts to lower temperature, which benefit from the doping of N and the increase of surface reactive oxygen. This also demonstrates the modification by HNO_3 improves the oxygen content of CB. After the loading of Au NPs, the TPR profile of HCB-Au shows that the reduction peaks further shift from 659.1 and 483.1°C to 649.0 and 452.6°C due to the cooperation of Au activating HCB. On the other hand, HCB-Ni_6 shows two stages on the TPR profile. The two peaks located at 433.9 and 533.5°C are assigned to the reduction of NiO strongly interacting with carbon. This result is similar to the findings reported by zhou et al. [55]. At the meantime, the increase for H_2 consumption of the peak at low temperature also demonstrate the enhancement between monometal and carbon support. Interestingly, the introduction of Au NPs into HCB-Ni_6 catalyst changes its property. As the TPR profile of HCB-Ni_6-Au_1 showed, two unsolved peaks co-locate with the maximum of H_2 consumption, which is associated with the reduction of the same species of HCB-Ni_6 catalyst. On the contrary, the relative proportions of the two peaks have been changed. The two peaks all become broad, the first peak increases in intensity and shifts to lower temperature around 373.8°C while the second peak obviously decreases in intensity and shifts to higher temperature around 543.1°C. These results suggest that the introduction of Au NPs facilitates the reduction of NiO, strongly interacting with the support. This finding coincides well with the study reported by Mierczynski et al. [44].

3.2. Catalytic performance for hydrogenation of nitrophenols

The catalytic performance of as-prepared monometallic and bimetallic nanocatalysts was investigated in the catalytic hydrogenation of 4-NP by $NaBH_4$ as model reaction. The absorption peak of 4-NP with ultrapure water in the UV-Vis spectra locates at 317 nm, and shifts at 400 nm with the addition of $NaBH_4$ (**Fig. S4**). The color of 4-NP also changes from light yellow to bright yellow (pictures inset of **Fig. S4**). This change is caused by the formation of nitrophenolate ions in alkaline solution because the pK_a of 4-NP is around 7.2 [40, 56]. In addition, the color does not change even for a month, which demonstrates the hydrogenation reaction cannot be triggered only in the presence of $NaBH_4$. However, after the addition of a small amount of HCB-Ni_6-Au_1 bimetallic nanocatlysts (5 mg), the absorption peak of 4-NP decreases rapidly while a new peak at 298 nm increases and the color changes to colorless subsequently, suggesting the generation of 4-AP (**Fig. S4** and **Fig. 4**). In the hydrogenation reaction, the amount of $NaBH_4$ is 50 times over than the amount of 4-NP (molar ratio). Thus, as reported by Wunder et al.[57], the hydrogenation reaction can be described by the pseudo-first order kinetics. The catalytic performance can be assessed by the apparent rate constant, k, and the value of it is depicted as the following equation [48]:

$$k = -\ln (C_t/C_0)/t \qquad (3)$$

where t is the reaction time, C_0 and C_t are the concentration of 4-NP at the beginning and at the reaction with different time, the values are related to the absorbance of 4-NP for the UV-Vis spectra, respectively.

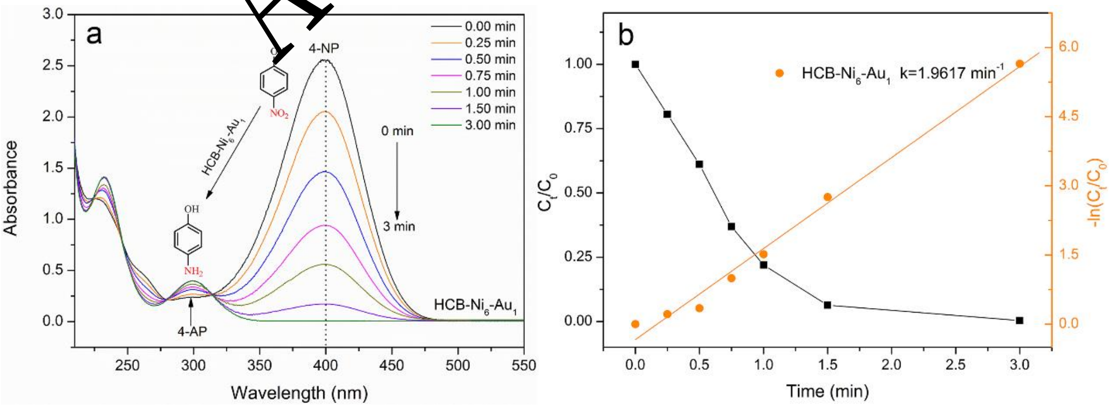

Fig. 4. UV-Vis spectra changing (a), plot of C_t/C_0, –ln (C_t/C_0) and pseudo-first-order kinetics fitting (b) for the hydrogenation of 4-NP by HCB-Ni_6-Au_1 bimetallic

nanocatalyst versus the reaction time.

In order to investigate the catalytic performance of prepared bimetallic nanocatalysts, a series of HCB-Ni-Au bimetallic nanocatalysts with different ratio of Ni and Au (2:1-10:1) are prepared and used for the hydrogenation of 4-NP. As shown in **Fig. S5**, with the increase of Ni/Au ratio, the catalytic activity of HCB-Ni-Au increases. Especially, the hydrogenation of 4-NP by HCB-Ni$_6$-Au$_1$ is almost complete within three minutes and HCB-Ni$_6$-Au$_1$ shows the highest catalytic activity with the k of 1.9617 min^{-1}. However, when the ratio increases over 6:1, the activity decreases inversely. This is possibly because large amount of Ni NPs reduce the pore structure of HCB. On the other hand, higher amount of Ni NPs may trend to aggregate because the anchor sites of HCB are not enough to disperse them completely. Meanwhile, the content of Au NPs may reduce. The corresponding reaction rate constants (k) and normalized reaction rate constants (k_{nor} = k/m, where m is the dosage of nanocatalysts) are summarized in **Table S3**. As comparison, the hydrogenation of 4-NP by HCB, HCB-Ni$_6$ and HCB-Au in the presence of NaBH$_4$ was proposed. As shown in **Fig. S6**, HCB shows no catalytic activity for the hydrogenation of 4-NP. HCB-Ni$_6$ and HCB-Au show obvious catalytic activity for the hydrogenation of 4-NP with the k of 0.1345 and 0.0511 min^{-1}, respectively. Although the catalytic activity of noble-metal nanocatalysts like Au-based catalysts is always higher than Ni-based nanocatalysts, the activity of HCB-Ni$_6$ here is much higher than HCB-Au due to the high content of Ni. Nevertheless, the activity of the HCB-Ni-Au bimetallic nanocatalytsts is much higher than both HCB-Ni$_6$ and HCB-Au. The activity of HCB-Ni$_6$-Au$_1$ is over even 14 and 38 times higher than HCB-Ni$_6$ and HCB-Au. This also demonstrates that the synergistic effect of Ni and Au play important role for the hydrogenation of 4-NP, which greatly enhances the catalytic activity. When compared with other reported studies, HCB-Ni$_6$-Au$_1$ exhibits high catalytic performance of 4-NP hydrogenation (**Table S4**). Additionally, the hydrogenation of 4-NP by HCB-Ni_6-Au_1 without $NaBH_4$ was investigated. As illustrated in **Fig. S7**, the absorption peak of 4-NP located at 317 nm only has slight decrease and no new peak at 298 nm has shown up in the absence of $NaBH_4$, illustrating the hydrogenation reaction can be processed only in the presence of both Ni or Au-based nanocatalysts and $NaBH_4$.

The contents of Ni and Au in prepared nanocatalysts were measured by ICP and the results are exhibited in **Table S3**. The measured and theoretically calculated values of them are close, which means the well deposition of Ni and Au on HCB. This also suggests the introduction of more O and doping of N by HNO_3 modification contribute to the anchoring of metal NPs, which is conducive to the improvement of catalytic activity. However, further increasing the ratio of Ni and Au, the difference between measured and theoretically calculated values of HCB-Ni-Au nanocatalysts is clearer. Interestingly, with the increase of Ni content, the content of Au increases in the beginning, while decreases when further improves the content of Ni. This suggests the presence of Ni NPs contributes to the formation of Au NPs. Nevertheless, the oxygen- and nitrogen-containing groups in HCB are not enough to further anchor more Ni and Au. This is consistent with the previous results.

3.3. Catalytic performance of different nitroaromatics

To further explore the general applicability of prepared HCB-Ni_6-Au_1 bimetallic nanocatlyst, the catalytic hydrogenation of other nitroaromatics was proposed. The catalytic performances like reaction time and reaction rates, as well as the molecular formulas and color changes of them are shown in **Table S5**. As observed from **Table S5**, all of the nitroaromatics can be catalyzed by HCB-Ni_6-Au_1 in 10 min and the color of them also changes to colorless, indicating a complete hydrogenation of them. The

UV-Vis spectra of 2-NP, 3-NP, MO, EBT, and CR show the absorption peaks at 414 nm, 393 nm, 466 nm, 613 nm, and 492 nm respectively, which decreased gradually with the proceeding of catalytic reaction. The catalytic rate constants of them follow the order: MO > 4-NP > EBT > 2-NP > 3-NP > CR. In this case, the catalytic rate constants for hydrogenation of nitrophenols follow the order of 4-NP > 2-NP > 3-NP is in good agreement with the reported papers [40, 58], which is mainly related to the inductive effect, conjugation effect, steric effect and/or molecular hindrance of nitrophenols to penetrate into the catalysts. To explain this phenomenon, DFT-computed relative Gibbs free energy of nitrophenols (2-NP, 3-NP, and 4-NP) are shown in **Fig. 5**. The ΔG of 3-NP is the lowest, which means the molecular geometry structure of 3-NP is more stable than the others. Hence 3-NP is supposed as the reference substance (ΔG is supposed to be 0 kcal mol^{-1}) to calculate the relative free energy of 2-NP and 4-NP. The calculated ΔG of 4-NP and 2-NP is 2.3 and 1.1 kcal mol^{-1}, which suggests the molecular geometry structure stability of 4-NP is lower than 2-NP and 3-NP, indicating 4-NP is easier to be catalyzed by HCB-Ni_6-Au_1. Thus, the reaction rates of nitrophenols follow the order of 4-NP > 2-NP > 3-NP, which well conforms to the experimental results.

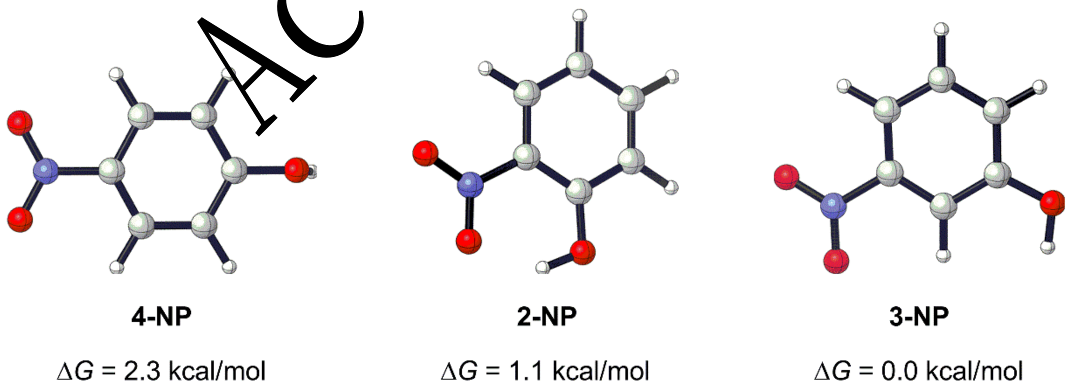

Fig. 5. DFT-computed relative Gibbs free energy profiles and structure model of 2-NP, 3-NP, and 4-NP. Energies are in kcal mol^{-1}.

In general, the catalytic activity in nitroaromatics hydrogenation with complicated structure is lower than that with simpler structure. In this study, the catalytic rate of

EBT is lower than the catalytic rate of 4-NP, while that of MO is much higher than the others. As described by Arrhenius equation (equation 4) [59],

$$\mathrm{Ln}\, k = \ln A - (E_a/RT) \tag{4}$$

where A is the Arrhenius constant, E_a is the activation energy, R is the general gas constant, and T is the temperature in Kelvin scale, the catalytic rate is determined by E_a and will decrease with the increase of the value of E_a when R and T are the same. In this study, E_a of the theoretical hydrogenation reaction process was calculated by a series of DFT calculation. Relative activation of enthalpy (Δ_rH) is calculated to represent E_a, in which R and T are the same. The values of Δ_rH for hydrogenation of 4-NP, MO, EBT, and CR are -126.9, -65.7, -76.2, and -128.2 kcal mol^{-1}, respectively, which indicates the hydrogenation reaction is spontaneous (**Fig. 6**a, c-e). Generally, the catalytic rate is theoretically assessed by the absolute value of Δ_rH ($|\Delta_rH|$). It is indicated that the higher the value of $|\Delta_rH|$ is, the higher the energy is required for the reaction proposing, which suggests the reaction rate is lower. In this study, the values of $|\Delta_rH|$ for hydrogenation of 4-NP, MO, EBT, and CR follow the order of CR > 4-NP > EBT > MO, which suggests the reaction rates should follow the order of MO > EBT > 4-NP > CR. This calculated result for the reaction rate of EBT and 4-NP is opposite with the experimental results. As shown in **Fig. 6**a and d, the hydrogenation of 4-NP proceeds by three mole of H_2, while hydrogenation of EBT needs two mole of H_2. Hence, the Δ_rH for 4-NP hydrogenation proceeded by two mole of H_2 to generate **INT1** was calculated (Δ_rH_1', **Fig. 6**b). Result shows that Δ_rH_1' is -74.8 kcal mol^{-1} and the $|\Delta_rH_1'|$ is higher than that of EBT hydrogenation. It indicates the catalytic rate of 4-NP is higher than that of EBT, which is good consistent with the experimental results.

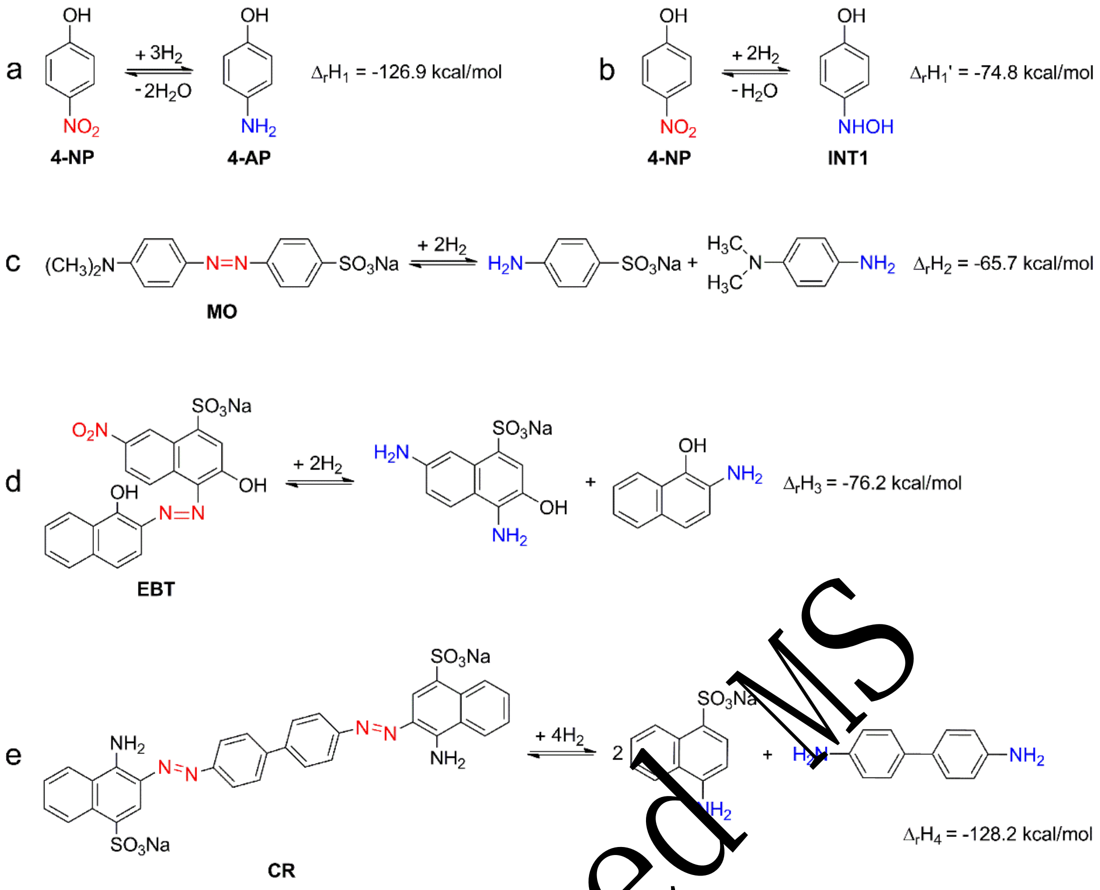

Fig. 6. The theoretical hydrogenation reaction process and corresponding activation enthalpy (Δ_rH) for 4-NP (a-b), MO (c), EBT (d), and CR (e).

3.4. Effect of pH and inorganic anions on the catalytic performance

The effect of pH on the catalytic activity of HCB-Ni_6-Au_1 for hydrogenation of 4-NP was proposed. The pH of 4-NP solutions was adjusted by 0.1 M HCl and NaOH and the initial pH of 4-NP in ultrapure water is about 5. As displayed in **Fig. 7**, the hydrogenation of 4-NP by HCB-Ni_6-Au_1 is highly dependent on pH values, in which lower pH provides higher catalytic activity. With the increase of pH values from 3-9, the catalytic activity decreases from 2.7140 min^{-1} to 0.7001 min^{-1}. In order to investigate the reason for this phenomenon, the pH_{IEP} of HCB-Ni_6-Au_1 was measured. As shown in **Fig. S8**, the Zeta potential of HCB-Ni_6-Au_1 goes from positive to negative with the pH increases from 1.5 to 9, which means the pH_{IEP} of is about 2. This further illustrates that the surface of HCB-Ni_6-Au_1 is negatively charged at pH > 2. In other words, the surface of HCB-Ni_6-Au_1 is more and more negatively charged from 3 to 9. Since the hydrogenation of 4-NP by HCB-Ni_6-Au_1 with excess $NaBH_4$ follows the Langmuir-Hinshelwood kinetics and adsorption is the first step, negatively charged BH_4^- is not easily adsorbed onto the surface of HCB-Ni_6-Au_1 at high pH due to the electrostatic repulsion, resulting decreased catalytic efficiency for hydrogenation of 4-NP. In addition, it is reported that the pK_a value of 4-NP is about 7.2, which means that 4-NP would primarily present in cationic state when the solution pH < pK_a [40]. Therefore, the adsorption of 4-NP with cationic state on the surface of negatively charged HCB-Ni_6-Au_1 would increase under acidic condition, resulting in highly enhanced catalytic efficiency. This explains the increased catalytic efficiency of 4-NP hydrogenation as the pH decreases, and indicates that adsorption plays an important role in the catalytic performance for 4-NP hydrogenation.

Inorganic ions always coexist with organics in real water body and may affect the catalytic activity of HCB-Ni_6-Au_1 in practical application. **Fig. 7** displays the effect of different ions on the catalytic efficiency and reaction rate of 4-NP by HCB-Ni_6-Au_1. As shown in **Fig. 7**c, the presence of CO_3^{2-} significantly inhibits the catalytic efficiency of 4-NP and only 20% of 4-NP is reduced to 4-AP within 3 min, while over 90% of 4-NP is reduced in the presence of other ions. This is possibly because the presence of CO_3^{2-} consumes the proton (H^+) of H_2O, produces HCO_3^- and H_2CO_3 and increases the pH of 4-NP (equation 5-6). On one hand, the consumption of H^+ inhibits the hydrolysis reaction of $NaBH_4$ to produce activation hydrogen (i.e. $H^\bullet$ radical species) (equation 7), thus lowering the catalytic efficiency. On the other hand, the increase of pH weakens the adsorption of 4-NP, which further limits the catalytic activity of HCB-Ni_6-Au_1. Interestingly, the addition of Cl^- slightly accelerates the catalytic efficiency with the k of 2.0285 min^{-1}, while the presence of SO_4^{2-} obviously limits the catalytic efficiency with the k of 0.9709 min^{-1}. The results are in good agreement with the findings reported by Nguyen et al. [40]. In addition, the addition of Ca^{2+} and Mg^{2+} has ignorable effect on the catalytic efficiency with the reaction rates of 1.9602 min^{-1} and 1.9381 min^{-1} respectively.

$$CO_3^{2-} + H_2O \leftrightarrow HCO_3^- + OH^- \quad (5)$$

$$HCO_3^- + H_2O \leftrightarrow H_2CO_3 + OH^- \quad (6)$$

$$BH_4^- + 2H_2O \rightarrow BO_2^- + 8H^{\cdot} \quad (7)$$

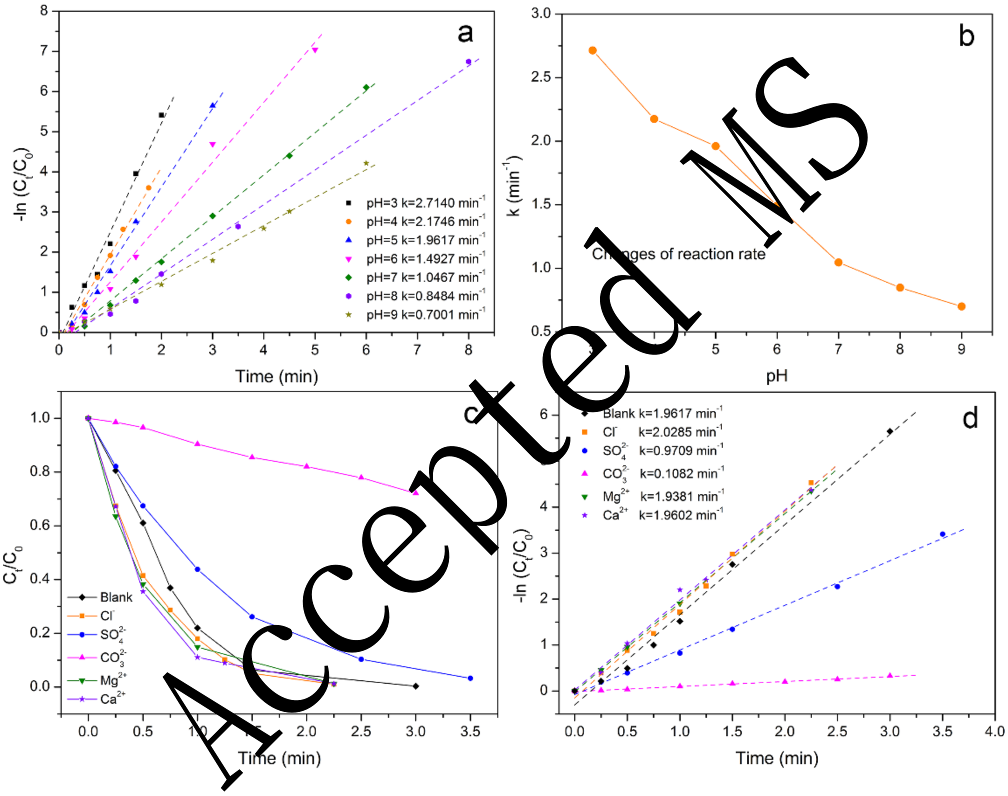

Fig. 7. Plots of -ln (C_t/C_0) versus reaction time (a) and changes of reaction rate (b) for the catalytic hydrogenation of 4-NP by HCB-Ni_6-Au_1 under different pH; Plots of C_t/C_0 (c) and -ln (C_t/C_0) (d) versus reaction time for the catalytic hydrogenation of 4-NP by HCB-Ni_6-Au_1 with different ions, including Cl^-, SO_4^{2-}, CO_3^{2-}, Mg^{2+} and Ca^{2+} (0.1 M).

3.5. Application of real water samples

The catalytic efficiency application on real water is very important for one catalyst. In this case, hydrogenation of 4-NP loading on distilled water, tap water, river water and lake water was proposed to assess the practicability of HCB-Ni_6-Au_1. The UV-Vis spectra of these samples were detected firstly to confirm the initial concentration of 4-NP and then the concentration of 4-NP was adjusted to 0.2 mM. As shown in **Fig. S9**, the absorption peaks of these water samples with 4-NP in UV-Vis spectra are all present at 400 nm and the colors of them are bright yellow, due to the pH values of them are higher than the pK_a of 4-NP (**Table S6**). In addition, after the addition of HCB-Ni_6-Au_1 and $NaBH_4$, a nearly complete conversion of 4-NP in all water samples is observed within 7 min, and the catalytic rates follow the order of distilled water > lake water > tap water > river water (**Fig. 8**). It is reported that the presence of dissolved oxygen (DO) may consume $NaBH_4$ and reduce the catalytic efficiency [60]. Hence, the concentration of DO in these samples was detected. As displayed in **Table S6**, the concentration of DO in distilled water is higher than the others, but the catalytic rate of distilled water is the highest. To further investigate this phenomenon, the concentration of Cl^-, SO_4^{2-}, CO_3^{2-}, Mg^{2+} and Ca^{2+} in these samples was further detected. Results show that there is no Cl^-, SO_4^{2-}, and CO_3^{2-} was found in distilled water, while a certain amount of Cl^- and SO_4^{2-} was found in other samples. As mentioned above, the presence of Cl^- and SO_4^{2-} can separately accelerate and inhibit the catalytic activity of HCB-Ni_6-Au_1. In this case, the concentration of Cl^- in tap water, river water and lake water is close and low but the concentration of SO_4^{2-} in river water is much higher than the others. It is reasonable that the catalytic rate of river water is the lowest.

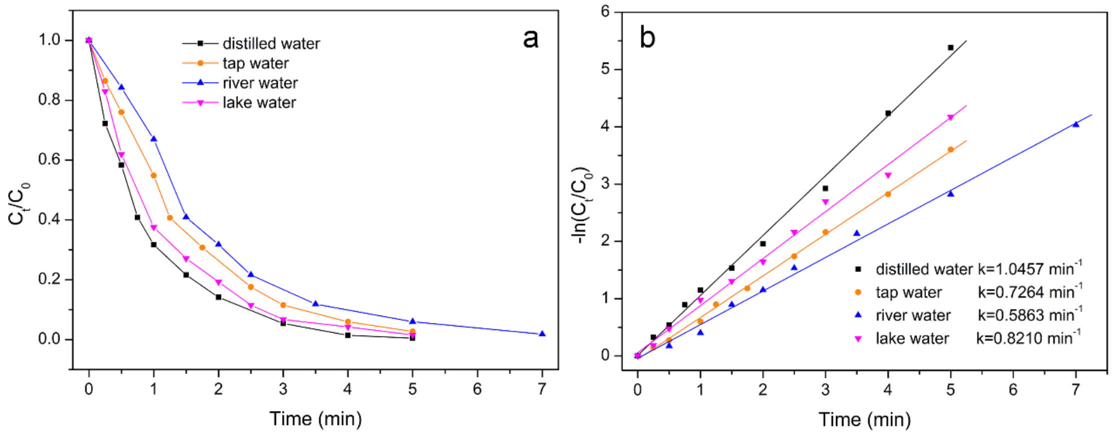

Fig. 8. Plots of C_t/C_0 (a) and -ln (C_t/C_0) (b) versus reaction time for the hydrogenation of 4-NP by HCB-Ni_6-Au_1 in distilled water, tap water, river water, and lake water.

3.6. Stability and recyclability

To investigate the stability and recyclability, HCB-Ni_6-Au_1 was reused in 8 repeated injections of 0.2 mM 4-NP. It is obvious that a nearly complete conversion of 4-NP to 4-AP by HCB-Ni_6-Au_1 and $NaBH_4$ can be rapidly achieved in 3 min and only 5% of catalytic efficiency decreases after 8 cycles of continuous usage (**Fig. 9**). Additionally, the crystal phase composition and elements analysis for HCB-Ni_6-Au_1 after 8 cycles were also examined. The analysis of XRD patterns confirms the occurrence of the same crystal phases of C, Ni NPs and Au NPs (**Fig. 10**a). Analysis of XPS spectra also demonstrates that the elemental composition and valence state of these elements in HCB-Ni_6-Au_1 after reaction is similar to that of the virgin HCB-Ni_6-Au_1. Interestingly, in high-resolution spectra for Au 4f, the peak of Au(III) oxidation state at 90.45 eV disappears and the peak of Au^0 is higher and broader in HCB-Ni_6-Au_1 after reaction. This is possibly because the presence of $NaBH_4$ reduces Au(III) to Au^0. In addition, the contents of Ni and Au measured by ICP are 12.51% and 0.56% respectively after 8 cycles, which just has a small loss compared with the virgin HCB-Ni_6-Au_1. In general, the above results illustrate HCB-Ni_6-Au_1 bimetallic nanocatalyst is structurally stable with high catalytic efficiency and good recyclability.

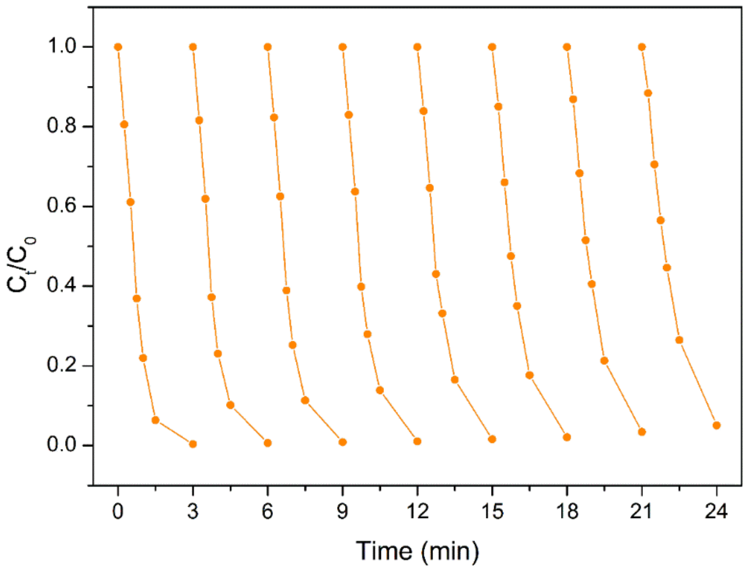

Fig. 9. Recyclability for the hydrogenation of 4-NP by HCB-Ni$_6$-Au$_1$ over 8 times.

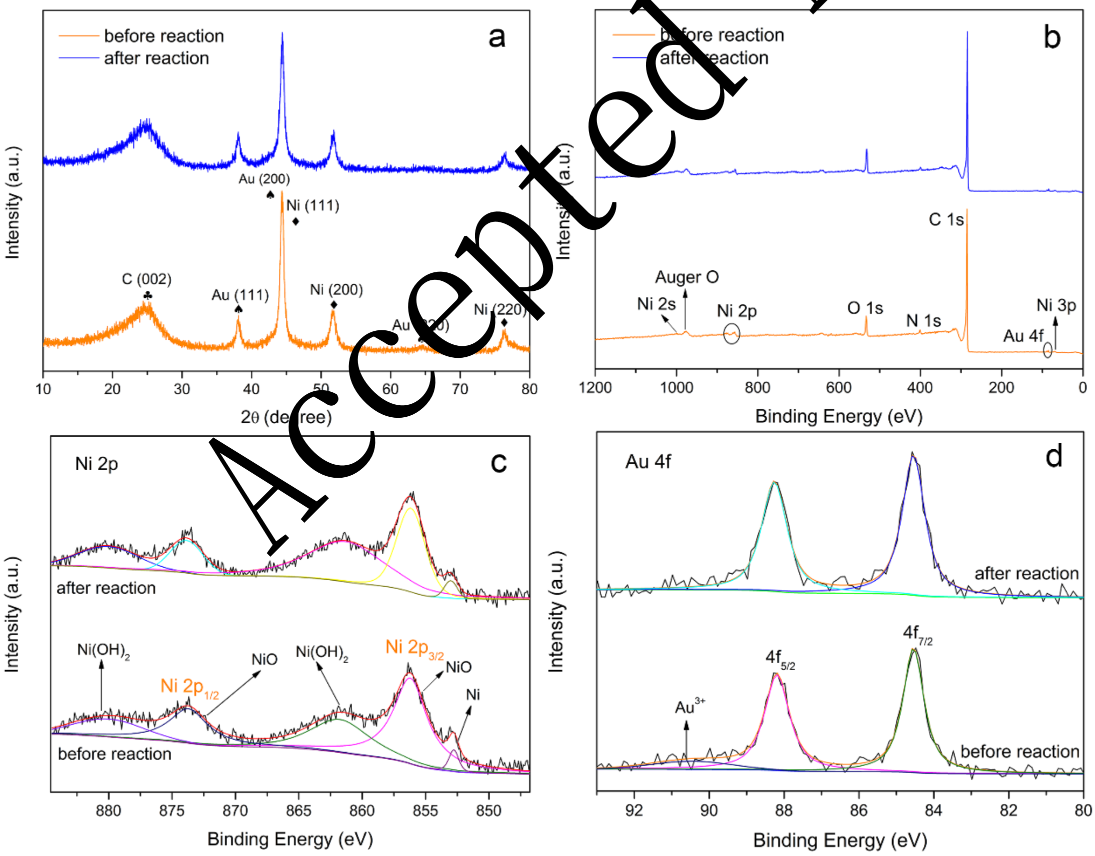

Fig. 10. XRD patterns (a), XPS survey spectra (b), and high-resolution spectra for Ni 2p (c) and Au 4f (d) of HCB-Ni$_6$-Au$_1$ bimetallic nanocatalyst before and after reaction.

3.7. Possible mechanism for the hydrogenation of nitroaromatics by HCB-Ni_6-Au_1 bimetallic nanocatalyst

According to the kinetics studies and relevant literatures, the mechanism for the hydrogenation of nitroaromatics by HCB-Ni_6-Au_1 bimetallic nanocatalyst is proposed on the basis of the Langmuir–Hinshelwood mechanism. As displayed in **Scheme 2**, using 4-NP hydrogenation as example, the hydrogenation process by HCB-Ni_6-Au_1 bimetallic nanocatalyst usually includes three steps: 1) 4-NP is adsorbed to the catalyst surface; 2) amounts of $H^\bullet$ radical species are produced by $NaBH_4$ reacts with H_2O and then they transfer to Ni and Au surface to form a nickel and gold hydride complex (i.e., Ni-H and Au-H); 3) the hydrogen transfers from Ni-H and Au-H to 4-NP. To further understand the reaction mechanism, EPR measurement with 5, 5-Dimethylpyrroline N-oxide (DMPO) as spin trapper was proposed to demonstrate the presence of $H^\bullet$ radical species and Ni-H and Au-H bonds. As displayed in **Fig. S10**a, a high signal intensity of nine-line surface plasmon resonance (SPR) spectrum is observed in the field of 3460-3560 G when $NaBH_4$ was added into the solution of 4-NP + HCB-Ni_6-Au_1 + DMPO. The spectra are composed by a 1:1:1 triplet of 1:2:1 triplets with $a_H = 22.57$ G and $a_N = 16.62$ G, which suggests the production of large amount of $H^\bullet$ radical species [40]. Besides, no signal is detected without $NaBH_4$, which means the $H^\bullet$ radical species are mainly generated by $NaBH_4$ (0 min). However, with the reaction processed versus time, the signal intensity is higher than the beginning. This demonstrates the presence of HCB-Ni_6-Au_1 bimetallic nanocatalyst facilitates the production of $H^\bullet$ radical species and formation of metal-H bond. As the previous papers, we have demonstrated the existence of Au-H bond in the hydrogenation of 4-NP. Thus, to prove the generation of Ni-H bond, the EPR measurement in the presence of HCB-Ni_6 monometallic nanocatalyst was also proposed. The results are similar with the measurement in the presence of HCB-Ni_6-Au_1 bimetallic nanocatalyst (**Fig. S11**), but the signal intensity is lower than that of HCB-Ni_6-Au_1 bimetallic nanocatalyst in 2 min, which demonstrates the generation of Ni-H bond (**Fig. S10**b).

To investigate the possible pathways of 4-NP and azo dyes (MO, CR, and EBT) degradation by $NaBH_4$ and HCB-Ni_6-Au_1, the degradation products were detected by a liquid chromatography-mass spectrometry (LC-MS). The LC-MS spectra of 4-NP and corresponding products during catalytic reaction (0, 1, and 2 min) are shown in **Fig. 11**a. In **Fig. 11**a, a peak is observed at 138 m/z, ascribed to the molecular formula of $C_6H_5NO_3$, namely 4-NP. After 1 min of catalytic reaction, a new peak at 108 m/z shows up corresponding to the molecular formula C_6H_7NO, which means the generation of 4-AP. Further, another two peaks at 122.1 and 124.1 m/z are detected corresponding to the molecular formula $C_6H_5NO_2$ and $C_6H_7NO_2$, which may be attributed to the generation of 4-nitrosophenol and hydroxylamine derivatives. Thus, the possible pathway of 4-NP degradation by HCB-Ni_6-Au_1 is proposed in **Fig. 11**b. Typically, the –N=O bond of 4-NP is attacked by 2H and one molecule of H_2O is lost from 4-NP to form 4-nitrosophenol. Subsequently, the –N=O bond of 4-nitrosophenol is cleaved and 2H are added to form –NHOH bond. Finally, the –N=O is further attacked by 2H and 4-NP is generated after losing another molecule of H_2O. This pathway is similar with the reported papers [49, 61]. As shown in **Fig. S12**a, the main signals of LC-MS spectra over MO degradation are located at 172.179 and 136.184 m/z, suggesting the possible products of $C_6H_6NO_3S^-$ and $C_8H_{12}N_2$. This also indicates the –N=N– bond in MO was possibly attacked by $H^•$ to form $–NH_2$, thereby inducing the degradation of MO (**Fig. S12**b). The LC-MS spectra of CR degradation show two peaks at 237.25 and 184.228 m/z, which indicates the probable generation of $C_{10}H_9N_2SO_3^-$ and $C_{12}H_{12}N_2$ (**Fig. S13**a). Similar with the possible pathway of MO degradation, the degradation of CR is due to the break of –N=N– bonds (**Fig. S13**b). In addition, the possible degradation pathway of EBT is similar with that of 4-NP and MO, in which it mainly depends on the cleavage of –N=O bond and azo linkage (–N=N–) to obtain $-NH_2$ (**Fig. S14**).

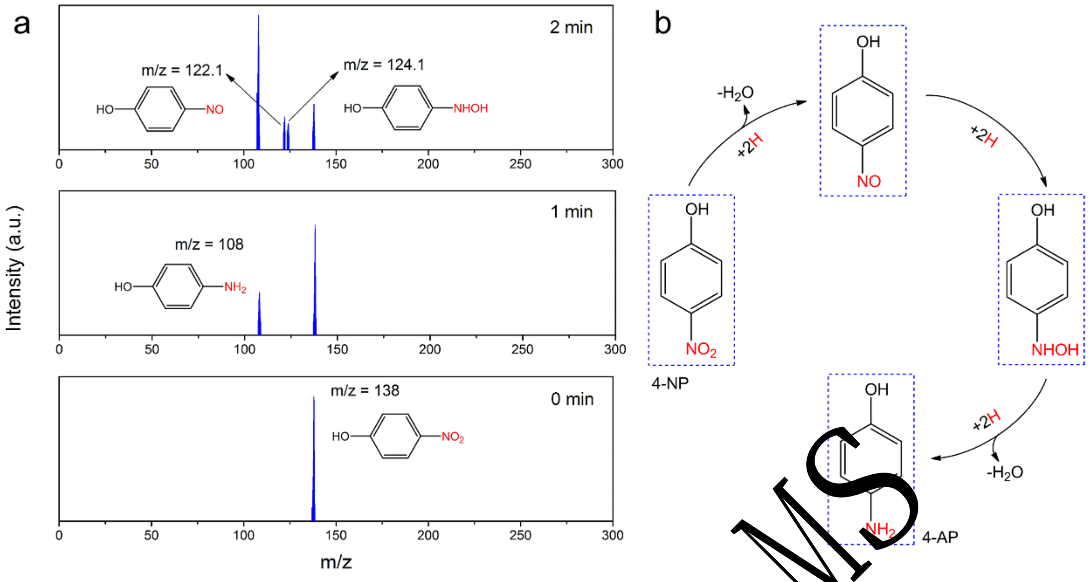

Fig. 11. LC-MS spectra of 4-NP and corresponding products during catalytic reaction (a) and possible pathway of 4-NP degradation catalyzed by HCB-Ni_6-Au_1 (b).

In this study, the high catalytic efficiency of prepared HCB-Ni_6-Au_1 bimetallic nanocatalyst can be attributed to two pairs of synergistic effects: 1) the support and metal NPs; 2) Ni NPs and Au NPs. For the synergistic effect between HCB and metal NPs, firstly, HNO_3 modified CB brings large amount of oxygen-containing groups and N-doping, which contributes to the improvement of hydrophilcity and dispersion of Ni NPs and Au NPs, as well as the stability of HCB-Ni_6-Au_1. Secondly, the modification by HNO_3 makes the hierarchical porous structure of CB become uniform, which is conductive to anchoring metal NPs on the surface, hence promoting the contact between nitroaromatics and active sites of HCB-Ni_6-Au_1. Thirdly, HCB with strong π–π stacking interaction provides strong adsorption of nitrophenols and dyes and fast electron transfer from HCB to Ni NPs and Au NPs, thus causing higher local electron densities and faster uptake of electron by nitrophenols and dyes. The catalytic activity is further improved. On the other hand, the introduction of oxygen-containing groups and N-doping is also beneficial to the adsorption of nitroaromatics, thus reducing the reaction time and promoting the catalytic efficiency.

For the synergistic effect between Ni NPs and Au NPs, it can be attributed to the following aspects. Firstly, the surface and size effects for nanometer-sized Ni and Au ensure them have better phase stability. The formation of smaller size of Au NPs with higher effective surface area owing to the presence of Ni NPs improves the catalytic activity of HCB-Ni$_6$-Au$_1$ as it is widely-reported that the catalytic activity proportional to the total surface metal NPs [48, 62]. Secondly, the difference of electronegativity between Au (2.54) and Ni (1.91) can induce electron transfer from Ni to Au leading to the generation of electron poor and rich regions on the bimetallic surface. The creation of electronic effect between Ni and Au would cause higher electron uptake and increased electron transfer between target molecules and result in high catalytic activity of HCB-Ni$_6$-Au$_1$ [50]. Thirdly, a strong synergistic effect could be observed from the strong coupling of SPR of Au and lower electrochemical reduction potential of Ni, further enhancing the catalytic activity [53]. Most importantly, the presence of Ni-H and Au-H bond plays synergic role in the hydrogenation of nitroaromatics, which further promotes the catalytic activity of HCB-Ni$_6$-Au$_1$. In general, the prepared HCB-Ni$_6$-Au$_1$ bimetallic nanocatalyst overcomes the disadvantage of prepared monometallic nanocatalysts and provides high stability and catalytic activity for nitroaromatics hydrogenation.

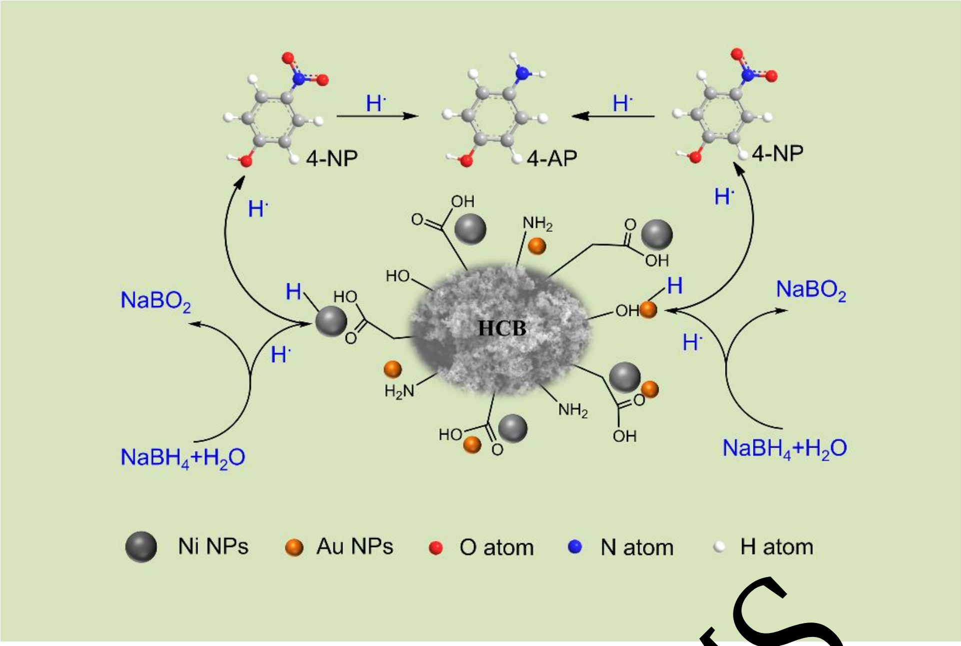

Scheme 2. Mechanism for hydrogenation of 4-NP by HCB-Ni$_6$-Au$_1$ in the presence of NaBH$_4$.

4. Conclusion

In this study, HCB-Ni-Au bimetallic nanocatalysts with different Ni/Au molar ratio were successfully synthesized for highly efficient hydrogenation of nitroaromatics. Modified CB with N-doping and abundant oxygen-containing groups is good candidate as support for anchoring metal NPs. The as-prepared HCB-Ni$_6$-Au$_1$ exhibits superior catalytic efficiency for the hydrogenation of nitroaromatics and the reaction for typical nitroaromatics follows the order of MO > 4-NP > EBT > 2-NP > 3-NP > CR. Besides, the catalytic activity for 4-NP is highly dependent on the initial pH of solution and anions concentration in reaction system. The reaction rate of 4-NP hydrogenation catalyzed by HCB-Ni$_6$-Au$_1$ reaches 1.9617 min^{-1}, which is 15 and 38 times higher than that of Ni and Au monometallic nanocatalyst respectively. HCB-Ni$_6$-Au$_1$ with good structural stability can be well reused and exhibits good catalytic activity on real water application. The mechanism, possible pathways, and catalytic efficiency of nitroaromatics hydrogenation were creatively investigated by combining DFT and some characterization techniques. The synergistic effect of Ni and Au on HCB with high catalytic efficiency overcomes the disadvantages of low catalytic efficiency of Ni-based nanocatalyst and high price of Au-based nanocatalyst and results in low usage of catalyst (5 mg) and $NaBH_4$ amount (10 mM). It provides a promising strategy for catalytic conversion in the field of water environment remediation. The combination of experiment and theoretical calculation technique is becoming a powerful strategy for today's science.

Acknowledgments

This study was financially supported by the Program for the National Natural Science Foundation of China (51879101, 51579098, 51779090, 51709101, 51521006, 51809090, 51278176, 51378190), the National Program for Support of Top–Notch Young Professionals of China (2014), the Program for Changjiang Scholars and Innovative Research Team in University (IRT-13R17), Hunan Provincial Science and Technology Plan Project (2018SK20410, 2017SK2243, 2016RS3026), the Fundamental Research Funds for the Central Universities (531119200086, 531118010114, 531107050978), and Hunan Provincial Innovation Foundation For Postgraduate (CX2018B155). The authors would like to thank Xiaobing Zhou from Shiyanjia Lab (www.shiyanjia.com) for the EPR analysis.

References

[1] C. Lai, M. Zhang, B. Li, D. Huang, G. Zeng, L. Qin, X. Liu, H. Yi, M. Cheng, L. Li, Z. Chen, L. Chen, Chem. Eng. J. 358 (2019) 891–902.

[2] X. Gong, D. Huang, Y. Liu, G. Zeng, R. Wang, J. Wan, C. Zhang, M. Cheng, X. Qin, W. Xue, Environ. Sci. Technol. 51 (2017) 11308-11316.

[3] X. Du, C. Li, L. Zhao, J. Zhang, L. Gao, J. Sheng, Y. Yi, J. Chen, G. Zeng, Appl. Catal. B: Environ. 232 (2018) 37-48.

[4] P. Xu, G.M. Zeng, D.L. Huang, C.L. Feng, S. Hu, M.H. Zhao, C. Lai, Z. Wei, C. Huang, G.X. Xie, Sci. Total Environ. 424 (2012) 1-10.

[5] B. Li, C. Lai, P. Xu, G. Zeng, D. Huang, L. Qin, H. Yi, M. Cheng, L. Wang, F. Huang, S. Liu, M. Zhang, J. Cleaner Prod. 225 (2019) 898-912.

[6] H. Yi, M. Yan, D. Huang, G. Zeng, C. Lai, M. Li, X. Huo, L. Qin, S. Liu, X. Liu, B. Li, H. Wang, M. Shen, Y. Fu, X. Guo, Appl. Catal. B: Environ. 250 (2019) 52-62.

[7] C. Lai, S. Liu, C. Zhang, G. Zeng, D. Huang, L. Qin, X. Liu, H. Yi, R. Wang, F. Huang, B. Li, T. Hu, ACS Sensors 3 (2018) 2566-2573.

[8] D. Huang, W. Xue, G. Zeng, J. Wan, G. Chen, C. Huang, C. Zhang, M. Cheng, P. Xu, Water Res. 106 (2016) 15-25.

[9] C. Zhang, W. Wang, A. Duan, G. Zeng, D. Huang, C. Lai, X. Tan, M. Cheng, R. Wang, C. Zhou, W. Xiong, Y. Yang, Chemosphere 222 (2019) 184-194.

[10] Y. Yang, C. Zhang, C. Lai, G. Zeng, D. Huang, M. Cheng, J. Wang, F. Chen, C. Zhou, W. Xiong, Adv. Colloid Interface Sci. 254 (2018) 76-93.

[11] B. Song, M. Chen, S. Ye, P. Xu, G. Zeng, J. Gong, J. Li, P. Zhang, W. Cao, Carbon 144 (2019) 1-7.

[12] S. Ye, M. Yan, X. Tan, J. Liang, G. Zeng, H. Wu, B. Song, C. Zhou, Y. Yang, H. Wang, Appl. Catal. B: Environ. 250 (2019) 78-88.

[13] L. Li, C. Lai, F. Huang, M. Cheng, G. Zeng, D. Huang, B. Li, S. Liu, M. Zhang, L. Qin, M. Li, J. He, Y. Zhang, L. Chen, Water Res. 160 (2019) 238-248.

[14] X. Ning, F. Wei, H. Fu, X. Qu, Z. Xu, S. Zheng, Appl. Surf. Sci. 445 (2018) 535-541.

[15] H. Wang, Z. Zeng, P. Xu, L. Li, G. Zeng, R. Xiao, Z. Tang, D. Huang, L. Tang, C. Lai, D. Jiang, Y. Liu, H. Yi, L. Qin, S. Ye, X. Ren, W. Tang, Chem. Soc. Rev. 48 (2019) 488-516.

[16] J.-L. Gong, B. Wang, G.-M. Zeng, C.-P. Yang, C.-G. Niu, Q.-Y. Niu, W.-J. Zhou, Y. Liang, J. Hazard. Mater. 164 (2009) 1517-1522.

[17] X. Zhou, C. Lai, D. Huang, G. Zeng, L. Chen, L. Qin, P. Xu, M. Cheng, C. Huang, C. Zhang, C. Zhou, J. Hazard. Mater. 346 (2018) 113-123.

[18] W. Xiong, Z. Zeng, G. Zeng, Z. Yang, R. Xiao, X. Li, J. Cao, C. Zhou, H. Chen, M. Jia, Y. Yang, W. Wang, X. Tang, Chem. Eng. J. 374 (2019) 91-99.

[19] K. He, G. Chen, G. Zeng, A. Chen, Z. Huang, J. Shi, T. Huang, M. Peng, L. Hu, Appl. Catal. B: Environ. 228 (2018) 19-28.

[20] Y. Yang, Z. Zeng, C. Zhang, D. Huang, G. Zeng, R. Xiao, C. Lai, C. Zhou, H. Guo, W. Xue, Chem. Eng. J. 349 (2018) 808-821.

[21] Z. Yan, L. Fu, X. Zuo, H. Yang, Appl. Catal. B: Environ. 226 (2018) 23-30.

[22] P. Ilgin, O. Ozay, H. Ozay, Appl. Catal. B: Environ. 241 (2019) 415-423.

[23] Y. Fu, P. Xu, D. Huang, G. Zeng, C. Lai, L. Qin, B. Li, J. He, H. Yi, M. Cheng, C. Zhang, Appl. Surf. Sci. 473 (2019) 578-588.

[24] L. Zhang, J. Zhang, G. Zeng, H. Dong, Y. Chen, C. Huang, Y. Zhu, R. Xu, Y. Cheng, K. Hou, W. Cao, W. Fang, Bioresour. Technol. 261 (2018) 10-18.

[25] Z. Huang, K. He, Z. Song, G. Zeng, A. Chen, L. Yuan, H. Li, L. Hu, Z. Guo, G. Chen, Chemosphere 211 (2018) 573-583.

[26] L. Qin, G. Zeng, C. Lai, D. Huang, C. Zhang, P. Xu, T. Hu, X. Liu, M. Cheng, Y. Liu, Sens. Actuators, B 243 (2017) 946-954.

[27] C. Lai, X. Liu, L. Qin, C. Zhang, G. Zeng, D. Huang, M. Cheng, P. Xu, H. Yi, D. Huang, Microchim. Acta (2017) 1-9.

[28] S. Ye, G. Zeng, H. Wu, C. Zhang, J. Dai, J. Liang, J. Yu, X. Ren, H. Yi, M. Cheng, C. Zhang, Crit. Rev. Biotechnol. 37 (2017) 1062-1076.

[29] C. Lai, Q. Lei, Z. Guangming, L. Yunguo, H. Danlian, Z. Chen, X. Piao, C. Min, Q. Xiangbin, W. Manman, Rsc Adv. 6 (2015) 3259-3266.

[30] L. Liu, R. Chen, W. Liu, J. Wu, D. Gao, J. Hazard. Mater. 320 (2016) 96-104.

[31] D. Huang, Z. Li, G. Zeng, C. Zhou, W. Xue, X. Gong, X. Yan, S. Chen, W. Wang, M. Cheng, Appl. Catal. B: Environ. 240 (2018) 153-173.

[32] S. Giri, R. Das, C.V.D. Westhuyzen, A. Maity, Appl. Catal. B: Environ. 209 (2017) 669-678.

[33] S. Chen, H. Fu, L. Zhang, Y. Wan, Appl. Catal. B: Environ. 248 (2019) 22-30.

[34] B. Li, C. Lai, G. Zeng, D. Huang, L. Qin, M. Zhang, M. Cheng, X. Liu, H. Yi, C. Zhou, F. Huang, S. Liu, Y. Fu, Small 15 (2019) 1804565.

[35] P. Song, L.-L. He, A.-J. Wang, L.-P. Mei, S.-X. Zhong, J.-R. Chen, J.-J. Feng, J. Mat. Chem., A 3 (2015) 5321-5327.

[36] C. Zhou, D. Huang, P. Xu, G. Zeng, J. Huang, T. Shi, C. Lai, C. Zhang, M. Cheng, Y. Lu, A. Duan, W. Xiong, M. Zhou, Chem. Eng. J. 370 (2019) 1077-1086.

[37] D. He, C. Zhang, G. Zeng, Y. Yang, D. Huang, L. Wang, H. Wang, Appl. Catal. B: Environ. 258 (2019) 117957.

[38] R. Das, V.S. Sypu, H.K. Paumo, M. Bhaumik, V. Maharaj, A. Maity, Appl. Catal. B: Environ. 244 (2019) 546-558.

[39] Y. Fu, T. Huang, B. Jia, J. Zhu, X. Wang, Appl. Catal. B: Environ. 202 (2017) 430-437.

[40] T.B. Nguyen, C.P. Huang, R.-a. Doong, Appl. Catal. B: Environ. 240 (2019) 337-347.

[41] L. Qin, H. Yi, G. Zeng, C. Lai, D. Huang, P. Xu, Y. Fu, J. He, B. Li, C. Zhang, M. Cheng, H. Wang, X. Liu, J. Hazard. Mater. 380 (2019) 120864.

[42] J. Xia, G. He, L. Zhang, X. Sun, X. Wang, Appl. Catal. B: Environ. 180 (2016) 408-415.

[43] X. Zhao, J. Zhu, L. Liang, C. Li, C. Liu, J. Liao, X. Wei, Appl. Catal. B: Environ. 154-155 (2014) 177-182.

[44] P. Mierczynski, K. Vasilev, A. Mierczynska, W. Maniukiewicz, M.I. Szynkowska, T.P. Maniecki, Appl. Catal. B: Environ. 185 (2016) 281-294.

[45] H. Wu, G. Pantaleo, V. La Parola, A.M. Venezia, X. Collard, C. Aprile, L.F. Liotta, Appl. Catal. B: Environ. 156-157 (2014) 350-361.

[46] X. Li, Y. Ma, Z. Yang, D. Huang, S. Xu, T. Wang, Y. Su, N. Hu, Y. Zhang, J. Alloys Compd. 706 (2017) 377-386.

[47] L. Qin, G. Zeng, C. Lai, D. Huang, P. Xu, C. Zhang, M. Cheng, X. Liu, S. Liu, B. Li, Coord. Chem. Rev. 359 (2018) 1-31.

[48] L. Qin, G. Zeng, C. Lai, D. Huang, C. Zhang, M. Cheng, H. Yi, X. Liu, C. Zhou, W. Xiong, F. Huang, W. Cao, Sci. Total Environ. 652 (2019) 93-116.

[49] Y. Fu, L. Qin, D. Huang, G. Zeng, C. Lai, B. Li, J. He, H. Yi, M. Zhang, M. Cheng, X. Wen, Appl. Catal. B: Environ. 255 (2019) 117740.

[50] M. Kumar, S. Deka, ACS App. Mat. Interfaces 6 (2014) 16071-16081.

[51] S. Navalon, R. Martin, M. Alvaro, H. Garcia, Angew. Chem. Int. Ed. 49 (2010) 8403-8407.

[52] D.S. Zheng, L.I. Hai-Rong, Y.Y. Wang, F.J. Zhang, Chin. J. Lum. 22 (2001) 351356.

[53] W.-Y. Chen, A. Matthews, F.R. Jones, K.-S. Chen, Surf. Coat. Technol. 336 (2018) 67-71.

[54] W. Xiong, Z. Zeng, X. Li, G. Zeng, R. Xiao, Z. Yang, H. Xu, H. Chen, J. Cao, C. Zhou, L. Qin, Chemosphere 232 (2019) 186-194.

[55] M. Zhou, L. Tian, L. Niu, C. Li, G. Xiao, R. Xiao, Fuel Process. Technol. 126 (2014) 12-18.

[56] J. Biswal, J. Paul, D.B. Naik, S.K. Sarkar, S. Sabharwal, Radiat. Phys. Chem. 85 (2013) 161-166.

[57] S. Wunder, F. Polzer, Y. Lu, Y. Mei, M. Ballauff, J. Phys. Chem. C 114 (2010) 8814-8820.

[58] L. Qin, D. Huang, P. Xu, G. Zeng, C. Lai, Y. Fu, H. Yi, B. Li, C. Zhang, M. Cheng, C. Zhou, X. Wen, J. Colloid Interface Sci. 534 (2019) 357-369.

[59] F. Naseer, M. Ajmal, F. Bibi, Z.H. Farooqi, M. Siddiq, Polym. Compos. 39 (2018) 3187-3198.

[60] E. Menumerov, R.A. Hughes, S. Neretina, Nano Lett. 16 (2016) 7791-7797.

[61] A. Corma, P. Concepción, P. Serna, Angew. Chem. 119 (2007) 7404-7407.

[62] Z. Zhang, C. Shao, P. Zou, P. Zhang, M. Zhang, J. Mu, Z. Guo, X. Li, C. Wang, Y. Liu, Chem. Commun. 47 (2011) 3906-3908.

[63] S. Duan, R. Wang, Prog. Nat. Sci. 23 (2013) 113-126.